



Effects of Annealing on the Fabrication of Al-TiAl₃ Nanocomposites Before and After Accumulative Roll Bonding and Evaluation of Strengthening Mechanisms

Zohreh Yazdani¹ · Mohammad Reza Toroghinejad¹ · Hossein Edris¹

Received: 13 May 2021 / Revised: 15 June 2021 / Accepted: 20 July 2021 / Published online: 26 August 2021
© The Chinese Society for Metals (CSM) and Springer-Verlag GmbH Germany, part of Springer Nature 2021

Abstract

The strengthening mechanisms of Al-TiAl₃ nanocomposite, fabricated using cold roll bonding, annealing, and accumulative roll bonding (ARB) on Al sheets sandwiching with pure Ti powder were investigated in the present study. With annealing at 590 °C for 2 h, TiAl₃ intermetallic compound was formed. After subsequent ARB process up to 5 cycles, final composite consists of ultrafine Al grains of less than 500 nm with TiAl₃ particles larger than 200 nm. The strength and hardness of the final composite are 2.5 and 3.5 times the initial values, with an ultimate tensile strength of 400 MPa, which is dominated by grain-boundary strengthening due to the ultrafine Al grains, and Orowan strengthening due to the small TiAl₃ particles. For comparison, an alternative fabrication route of cold roll bonding–ARB–annealing was also studied. This study showed that annealing before ARB is a critical factor in producing an ultrafine grain structure containing TiAl₃ particles.

Keywords Composite · Annealing · Strength · Microstructure · Al

1 Introduction

In the last few years, Al-based composites have gained increased notice on account of their low weight, high elastic modulus, and suitable electrical and magnetic properties, which have resulted in their modern and advanced applications in industries such as aerospace, military, and automotive [1]. In metal-matrix composites, the reinforcing phase should be selected to generate the required properties during manufacturing and preparation processes. Some of the essential properties of reinforcement particles include low density, matching thermal expansion coefficient with matrix, chemical compatibility, high elastic modulus, high tensile and compression strength, ease of manufacturing, and feasibility. The combination of these properties is often seen in non-metallic ceramic compounds [2].

Metal aluminides are intermetallic compounds that are suitable candidates for the strengthening of Al-matrix

composites. These compounds have densities close to those of ceramics but higher elastic modulus. More importantly, they are at thermodynamic equilibrium with the Al matrix [3], which means that they form strong chemical bonds with the Al matrix, contrary to ceramics that only have an intermediate reaction zone. Among aluminides, Ti aluminides such as TiAl₃ show high elastic modulus and melting points [3]. Composites containing TiAl₃ present cooperation of the high strength and low density of Ti aluminide and the high toughness of Ti or Al. Furthermore, the desirable high-temperature characteristics of aluminides are retained during the composite manufacturing process [4, 5].

Common methods for manufacturing metal-matrix composites include spray deposition, casting, and powder metallurgy. Among the common technologies used for the manufacturing of composite materials, a combination of cold roll bonding, accumulative roll bonding (ARB), and annealing has received significant interest compared to other methods recently because of its high efficiency and cost-effectiveness. Rolling can result in the formation of interatomic bonds between the two layers if they are connected through the initial contact surfaces without impurities. ARB is one of the severe plastic deformation (SPD) methods used to manufacture nanosized materials using great plastic strains. Comparing to other SPD methods, in the ARB method, there is no need to

Available online at <http://link.springer.com/journal/40195>.

✉ Zohreh Yazdani
z.yazdani@alumni.iut.ac.ir

¹ Department of Materials Engineering, Isfahan University of Technology, 84156-83111 Isfahan, Iran

shaping equipment with heavy load capacitance; besides, the quantity of metals fabricated is not restricted. In this process, 2 sheets with a thickness of t are placed on top of each other and undergo a rolling process with a 50% thickness reduction. The resulting 2-layered sheet with a thickness of t is then cut into 2 halves, which are then stacked all over each other and rolled another time. During this process, the strain is almost uniformly distributed among the grains, and repeating the process for a high number of cycles may lead to a uniform distribution of the reinforcing particles in the matrix [6–8]. The procedure allows the constant building of significant substances with ultra-fine grains but without any changes in geometric in the last sheets. There are several strengthening mechanisms that affect a material progressed by ARB. These involve strain hardening, grain refinement, redundant shear strain because of extreme deformation in the inside of the sheet, severe shear deformation at the subsurface, the creation of new interfaces, and distribution of inclusions and oxides at the interface.

Therefore, it is desirable to use cold roll bonding and ARB process for Al–Ti composites and then annealing to manufacture Al–matrix composites with an aluminide reinforcing phase [5]. In previous studies, rolling or ARB processes have frequently been used before annealing for the manufacturing of Ti aluminide compounds, including the manufacturing of TiAl and TiAl₃ sheets using hot rolling–annealing [9], γ -TiAl sheets through the cold roll bonding, subsequently annealing of Ti–Al foils at temperatures more than the melting temperature of Al [10], and a Ti aluminide alloy using ARB and annealing [11]. These studies indicate that the use of cold roll bonding or ARB processes creates dislocations and other crystalline defects, and therefore, facilitating reactions during the subsequent diffusion-based process and the formation of Ti aluminide compounds during the annealing stage. However, these methods are not capable of producing small grain sizes and suitable mechanical properties. Very few studies have investigated the manufacturing of Al composites using Ti aluminide reinforcement particles through cold roll bonding, ARB, and annealing. Consequently, the manufacturing of an Al–matrix nanocomposite with a Ti aluminide reinforcing phase using a cold roll bonding–annealing–ARB procedure was recently developed by the present authors [12]. In the current study, the effects of annealing before and after ARB on microstructure, mechanical properties, and strengthening mechanisms were investigated.

2 Experimental

Al 1100 sheets were employed for the manufacturing of the Al/Ti aluminide composite. These layers, with a thickness of 1 mm, were annealed at 350 °C for 1 h to remove their rolling history. Table 1 indicates the chemical analysis results of the initial Al sheets, and Table 2 shows their mechanical properties. Ti powder was obtained from Merck Co., Germany (99% purity). The scanning electron microscope (SEM) image of the Ti powder is provided in Fig. 1. As observed, the primary Ti powder has a non-uniform size distribution with an angular morphology (Fig. 1a, b). Because of the large particle size of the initial Ti powder (average 45 μ m) and to increase the adhesion of the powder particles throughout the roll bonding, the initial Ti powder underwent a mechanical ball milling process for 7 h with a constant disk spinning speed of 500 rpm, using 5 balls with a diameter of 2 cm made of ball-bearing steel. As a result of mechanical ball milling, the average Ti particle size declined to 0.8 μ m (Fig. 1c, d). The annealed Al sheets were cut into a dimension of 100 mm \times 50 mm, and holes were drilled into the 4 corners of each sheet. The sheets were then washed with hydrochloric acid and acetone before brushing to create a surface roughness of 3 μ m. To add Ti powder between the sheets, the Ti powder was first mixed with ethanol, and the resulting suspension was uniformly sprayed onto the surface of one of the sheets. After preparing the samples' surface, the rolling procedure was performed within less than 120 s to prevent the contamination of the surfaces. The roll bonding was performed at a spinning speed of 10 rpm. First, Al sandwiches containing 5 wt% of Ti were already prepared being rolled to 50% deformation. The rolled specimens were then heated at 590 °C for 2 h in an electrical furnace. To protect the samples from oxidation, they were placed in a container and covered with alumina powder. The container was then heated to the desired temperature and was cooled inside the furnace. The sample then underwent 5 cycles of the ARB procedure. For the ARB process, the sample from

Table 1 Chemical composition (wt%) of the Al sheets

Al	Si	Fe	Cu	Mn	Mg	Cr	Ni	Zn
99.05	0.156	0.710	0.133	0.047	0.030	0.015	0.038	0.037

Table 2 Mechanical properties of the Al sheets

Al condition	Tensile strength (MPa)	Yield strength (MPa)	Elongation	Hardness (HV)
As-received	157	142	7	48
Annealed	110	39	35	19

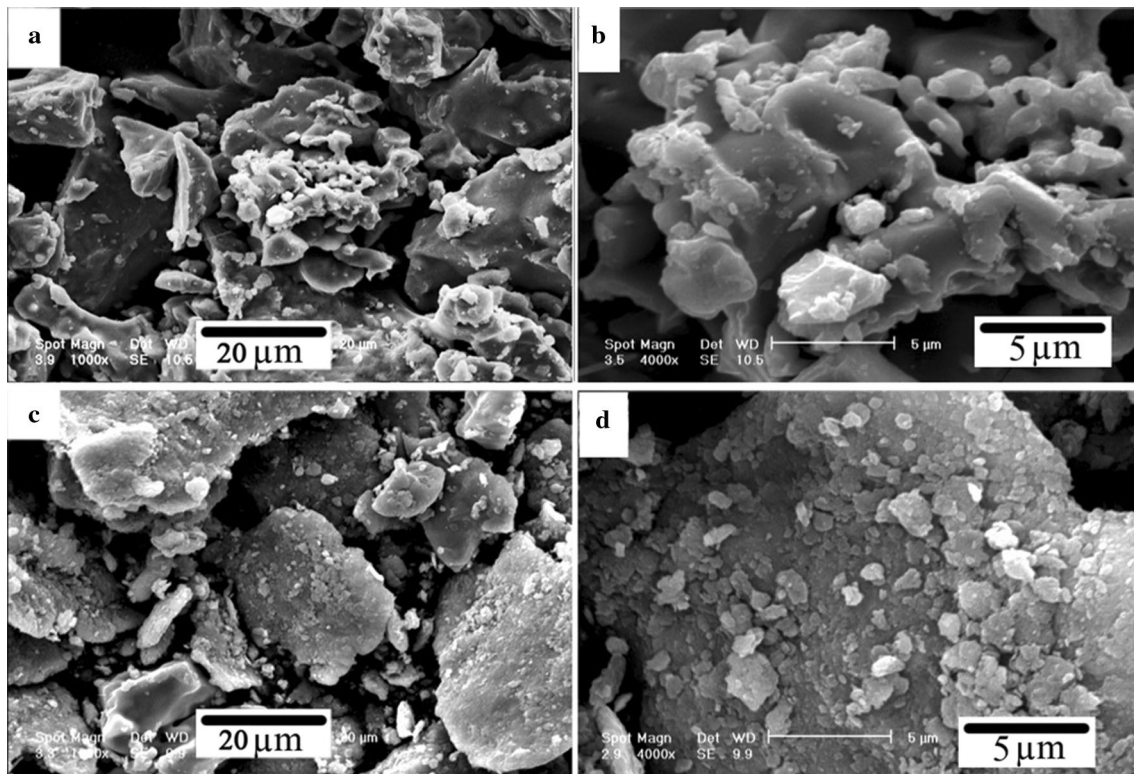


Fig. 1 SEM images of the Ti powder: **a, b** before, **c, d** after 7 h of ball milling

the previous cycle was cut at mid-length, drilled, and both surfaces were brushed, and the 2 pieces were fixed on top of each other by copper wires threading the drilled holes before rolling to 50% in the next cycle.

For easy understanding, in the following sections, cold roll bonding samples are denoted by CRB, cold roll bonding samples after annealing at 590 °C for 2 h are denoted by CRB-AT, and specimens after cold roll bonding, annealing at 590 °C for 2 h, and ARB for n cycles are marked CRB-AT-ARB n .

For comparison, some Al 1100 samples sandwiching 0.5 wt% of Ti powder also underwent up to 5 cycles of ABR process after CRB to 50%, but without the 590 °C annealing before the ABR as in the above-mentioned samples, and were then annealed under the same conditions to produce intermetallic compounds as mentioned in previous studies [10–13]. For simplicity, CRB samples to 50% deformation with ARB for n cycles are denoted by CRB-ARB n , and samples annealed at 590 °C for 2 h after the ARB process are indicated by CRB-ARB n -AT.

To evaluate the microstructures of the resulting phases and distribution of particles, the samples were examined using a field emission scanning electron microscope (FE-SEM) (Model S4800; Hitachi, Ibaraki, Japan) equipped with energy-dispersive X-ray spectroscopy (EDS) and a transmission electron microscope (TEM) (Tecnai G2 20

S-TWIN; FEI Company, USA). TEM specimens were prepared using electropolishing. The sub-surface areas of the specimens were prepared for SEM examination using focused ion milling (FIB) in SEM (Quanta 200-3D; FEI Company, USA) using a current of 20 nA to a depth of 1 μm . The hardness and elastic modulus of the Al matrix in specimens were measured using a nanoindenter (G200; Agilent Technologies, Inc., CA, USA) and the Oliver–Pharr method [14], with 16 repeated measurements in a 4 \times 4 matrix to obtain the average result in each condition.

Uniaxial tensile examinations were utilized to investigate the tensile behavior of the specimens. Tensile strength samples were prepared alongside the rolling direction, and the examinations were implemented at a rate of 1 mm/min.

The crystallite size (D) and micro-strain (ϵ) parameters, which are used for the calculation of dislocation density (ρ), are directly calculated from XRD data via the materials analysis using diffraction (MAUD) software. To this end, XRD patterns were matched with the graph calculated by the MAUD software until a goodness-of-fit (GOF) factor of less than 2 was obtained, which indicated the fit between the experimental pattern and the estimated graph. XRD tests were conducted using Philips X'PERTMPD equipment (Amsterdam, Netherlands) with a current of 30 mA and a voltage of 40 kV.

3 Results and Discussion

3.1 Distribution of TiAl₃ Particles in Al Matrix in CRB-AT-ARB and CRB-ARB-AT Composites

In the first manufacturing process, samples underwent ARB process after CRB and annealing at 590 °C for 2 h (the CRB-AT-ARB samples). According to our previous studies [15], the deformation threshold of the Al layers in the existence of 5 wt% of Ti particles in the initial CRB is 45%. Therefore, deformation of 50% was used in this case. Moreover, our previous results indicated that cold roll bonding with deformation of 50% and annealing would lead to the complete reaction between Al and Ti and finally, the generation of TiAl₃ intermetallic compound, and these roll bonding and annealing conditions are enough to convert total the added Ti into TiAl₃ [12]. In the third step of the manufacturing process of this composite, ARB was used to break the intermetallic particles which were still present at the interface of the two Al layers at the previous locations of the Ti particles and to create a uniform distribution of these particles in the matrix. In the ARB method, the constant plastic deformation also helps remove Kirkendall pores and improve the

mechanical features of the composite. Figure 2 demonstrates the SEM images of the composite after the 1, 3, and 5 cycles of the ARB procedure. As evidenced, after 1 cycle of ARB (Fig. 2a), the initial intermetallic particles with a size of less than 100 μm have started to break, resulting in a final microstructure containing 2 groups of small and large particles. Furthermore, there are areas without intermetallic particles in the Al matrix. However, with the implementation of subsequent ARB cycles, the intermetallic compound particles were broken, implementing a better distribution of the particles. The average particle size was less than 10 μm after 3 ARB cycles (Fig. 2b), and this decreased to 5 μm after 5 ARB cycles with no Kirkendall pores present (Fig. 2c).

In the second manufacturing process, samples underwent CRB and ARB process before being annealed at 590 °C for 2 h (the CRB-ARB-AT samples). The microstructures of the annealed CRB-ARB samples after 1, 3, and 5 ARB cycles are presented in Fig. 3. According to Fig. 3a, with 1 ARB cycle, some Ti particles have been transformed into the intermetallic compound as a result of annealing at 590 °C, resulting in the existence of large intermetallic particles with a size of more than 50 μm in the microstructure. After 3 ARB cycles and annealing at 590 °C for 2 h (Fig. 3b), smaller intermetallic particles were present in the microstructure,

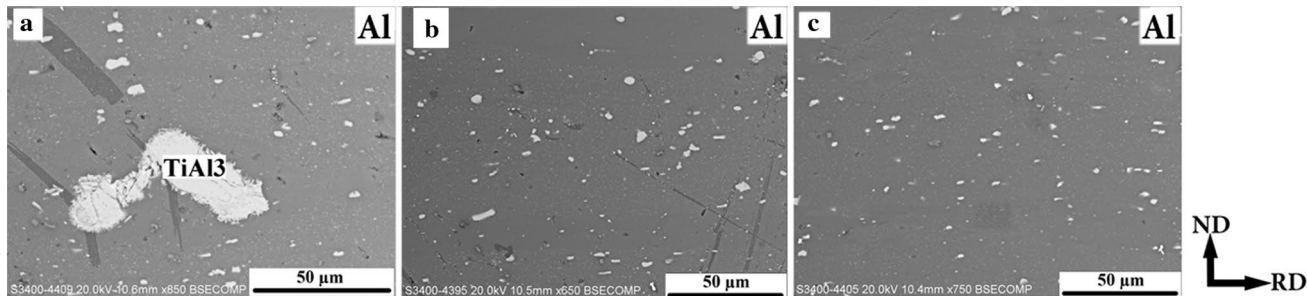


Fig. 2 SEM images of the distribution of TiAl₃ intermetallic particles after **a** one, **b** three, **c** five cycles of ARB procedure in the samples manufactured using cold roll bonding, annealing at 590 °C for 2 h, and ARB process (CRB-AT-ARB samples)

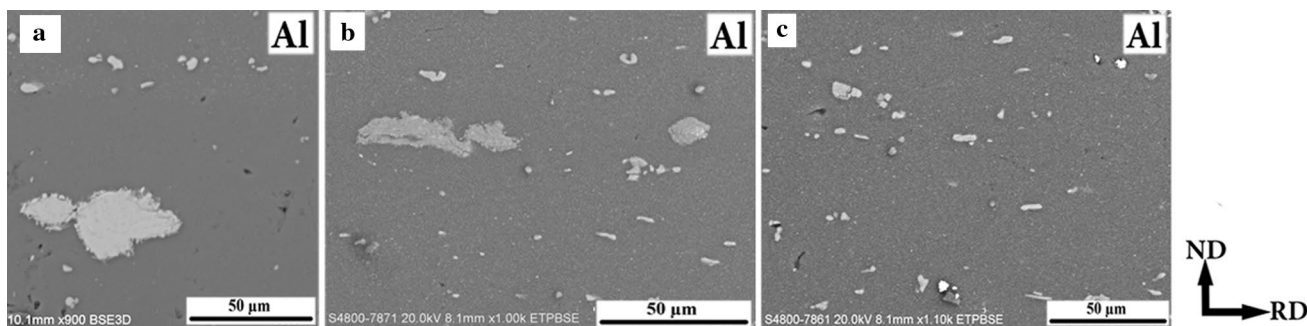


Fig. 3 SEM images exhibiting the distribution of TiAl₃ intermetallic compounds in samples manufactured using cold roll bonding, annealing at 590 °C for 2 h, and ARB process for **a** 1, **b** 3, **c** 5 cycles

and the distribution of particles had been improved. With further growth in the ARB cycles and after annealing (Fig. 3c), the size of the intermetallic particles decreased further, reaching nearly 10 μm , with a more uniform distribution. These results indicate that in both manufacturing methods, boosting ARB cycles resulted in a more uniform distribution of the reinforcement particles. Moreover, an enlargement of ARB cycles enhanced the number of layers, which resulted in better homogeneity in the particle distribution in the ND direction. Another reason for the more uniform particle distribution at higher ARB cycles is the severe plastic deformation beneath the surface of the sheet, which spreads toward the depths of the sheets with extending the ARB cycles [16].

For comparison, the SEM images of the CRB-AT-ARB5 and CRB-ARB5-AT samples (where the 5 denotes 5 ARB cycles) are displayed in Fig. 4 at a higher magnification. According to these images, using the ARB process after annealing and the formation of intermetallic particles (i.e., the CRB-AT-ARB5 sample in Fig. 4a) results in a more uniform particle size distribution as well as a smaller average particle size compared to performing ARB before annealing (Fig. 4b), which resulted in the presence of ultrafine intermetallic particles with sizes of less than 200 nm along with microns-large particles. In the CRB-ARB5-AT sample shown in Fig. 4b, TiAl_3 particles of various sizes are seen presumably because large Ti particles were present after 5 cycles of ARB before annealing.

3.2 TEM Microstructures of CRB-AT-ARB and CRB-ARB-AT Composites

Figure 5 demonstrates the microstructure of the CRB-AT-ARB1 composite sample with the equivalent strain (ϵ_{eq}) of 0.8. The TEM images, and the selected area diffraction (SAD) pattern of Fig. 5, were obtained from the TD-RD plane of the sample. According to Fig. 5a, under these

conditions, some Al grains are larger than 5 μm , which is due to the annealing process at 590 $^\circ\text{C}$ for 2 h before the ARB process. Figure 5b, c shows parts of the microstructure in which the ARB process has resulted in the plastic deformation of the previous fully annealed Al matrix. Moreover, the dark contrast between bright regions indicates the forming of low-angle grain boundaries containing dislocations, which are seen in the subgrain boundaries. The presence of reinforcement particles through the ARB method led to raising in dislocation density around the particle–matrix interfaces and the matrix as a result of the difference in deformability between the 2 phases.

The dislocation density (ρ) is calculated using the Smallman–Westmacott equation and crystallite size (D) and micro-stain (ϵ) [17]:

$$\rho = \frac{3\sqrt{2\pi}(\epsilon^2)^{1/2}}{Db}, \quad (1)$$

For the CRB-AT-ARB1 sample, the calculated dislocation density using Eq. (1) was $1.8 \times 10^{13} \text{ m}^{-2}$. However, the dislocation density of the CRB sample was $7 \times 10^{13} \text{ m}^{-2}$, and that of the CRB-AT sample was $3.6 \times 10^{13} \text{ m}^{-2}$. The SAD pattern of the Al matrix (Fig. 5d) shows dotted diffraction rings of the FCC structure with a lattice parameter of 4.05 \AA , while the limited spread of the (111) and (200) diffraction spots in the circumferential direction of the Debye–Scherrer rings indicates low misorientations between the grains making up the rings. Consequently, it can be assumed that in this step, the grain structure predominantly includes subgrains with a dislocation-cell structure.

Figure 6 exhibits the TEM images and a SAD pattern of the CRB-AT-ARB3 composite sample with the equivalent strain (ϵ_{eq}) of 2.4. According to Fig. 6a, large subgrains of nearly 1 μm are still present in the structure; in this Figure, geometrically necessary boundaries and TiAl_3 particles are referred to by black and white arrows, respectively. As

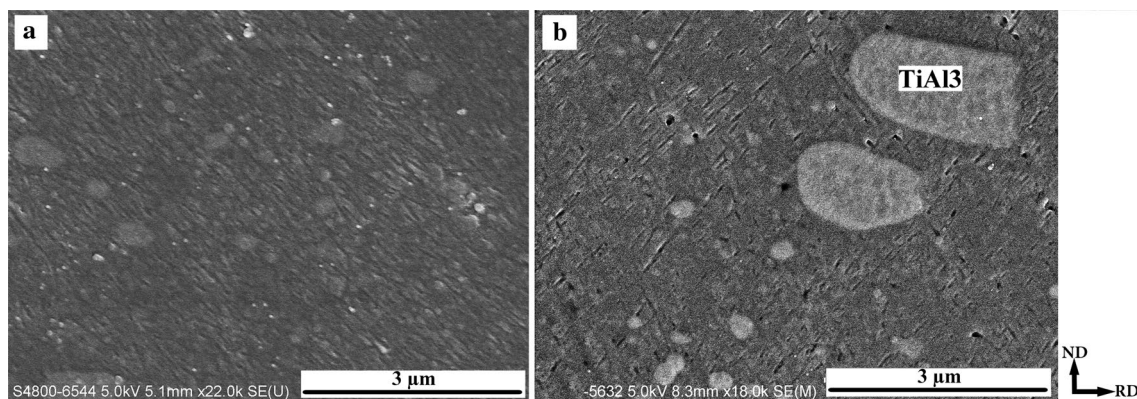


Fig. 4 SEM images displaying the distribution of TiAl_3 intermetallic particles in **a** CRB-AT-ARB5, **b** CRB-ARB5-AT

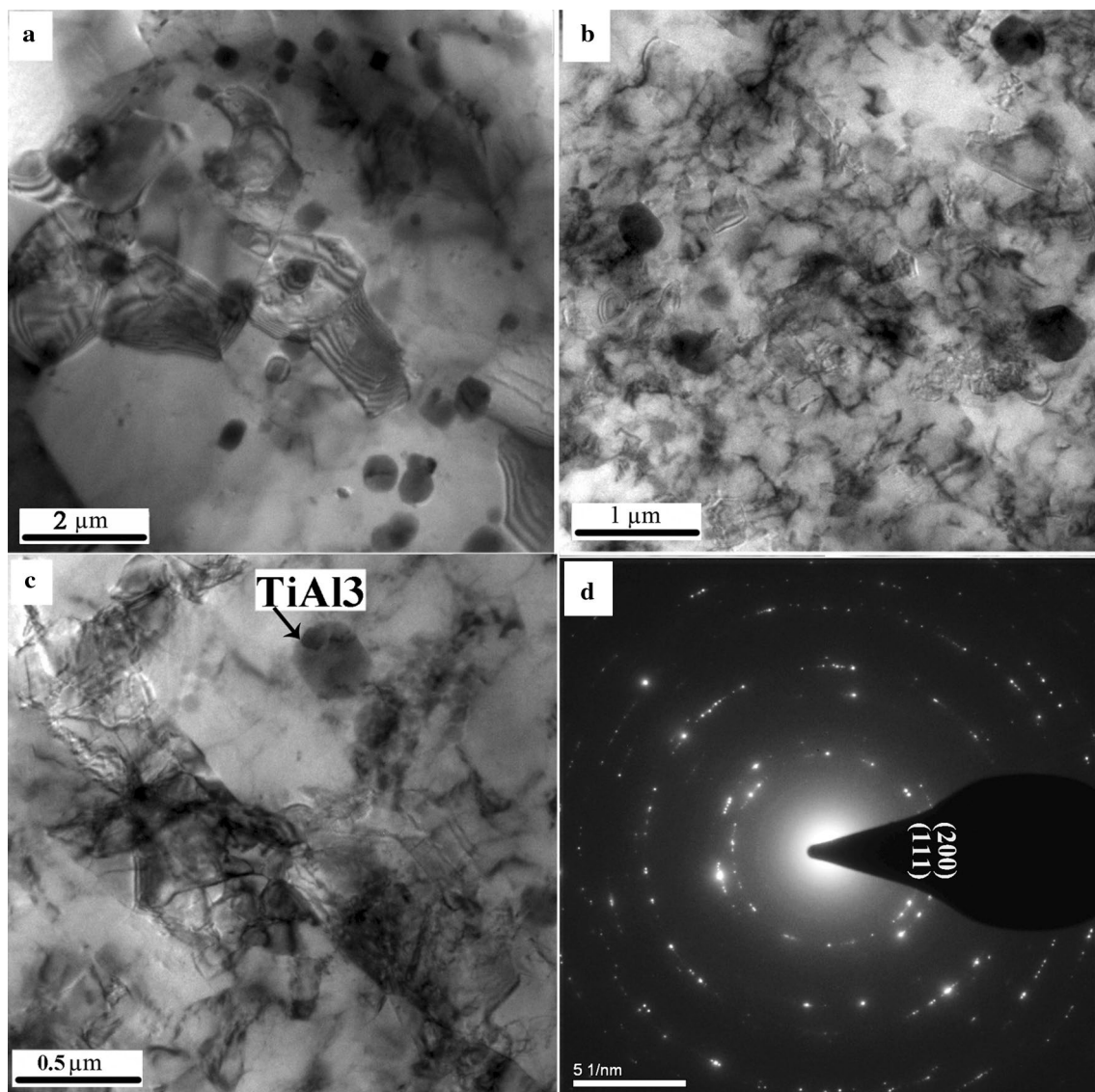


Fig. 5 TEM images of CRB-AT-ARB1 at different magnifications **a–c**, the relevant SAD pattern **d**

demonstrated, the average size of the intermetallic particles has reduced with expanding the proportion of ARB cycles, while the microstructure has to a great extent been converted into subgrains with an average size of less than 0.5 μm (Fig. 6b). The dislocation density in this sample increased compared to the previous sample (Fig. 5) and was calculated to be $10.8 \times 10^{13} \text{ m}^{-2}$. However, the dislocation density in the subgrains decreased with a reduction in subgrain size. This shows that dislocations have moved into grain boundaries, and so, the dislocation density inside the subgrains is lower. The SAD pattern of this specimen (Fig. 6c) shows dotted diffraction rings of the FCC pattern. This shows that the majority of grains are still subgrains with low-angle grain boundaries.

TEM images of the microstructure of CRB-AT-ARB5 composite with equivalent strain 4 along with its SAD pattern are presented in Fig. 7. The distribution of intermetallic compounds in Fig. 7a is clear and indicates a good distribution of intermetallic particles after the fifth ARB cycle. The calculated dislocation density of this sample was $45 \times 10^{13} \text{ m}^{-2}$. As can be observed in Fig. 7b, 5 cycles of the ARB procedure have resulted in an increased overall dislocation density, a decrease in dislocation density inside the cells, and a smaller subgrain size. The maximum subgrain size of the Al matrix, in this case, was 500 nm. The misorientation between subgrains and the ratio of ultrafine grain areas extended with ARB cycles. Images with higher magnification indicate that the average size of the intermetallic

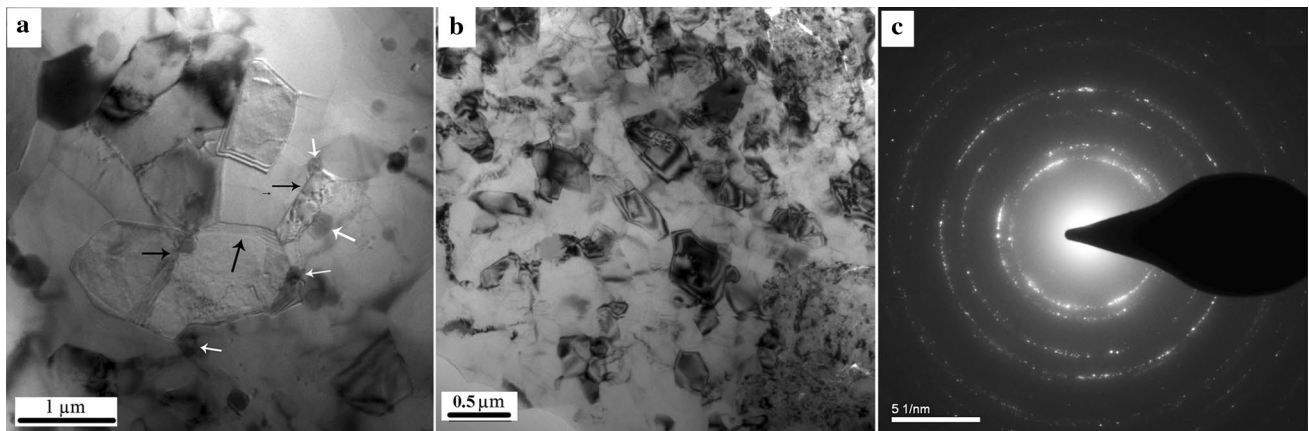


Fig. 6 TEM images of CRB-AT-ARB3 at different magnifications **a**, **b**, the relevant SAD pattern **c** (black and white arrows showing the geometrically necessary boundaries and intermetallic particles, respectively)

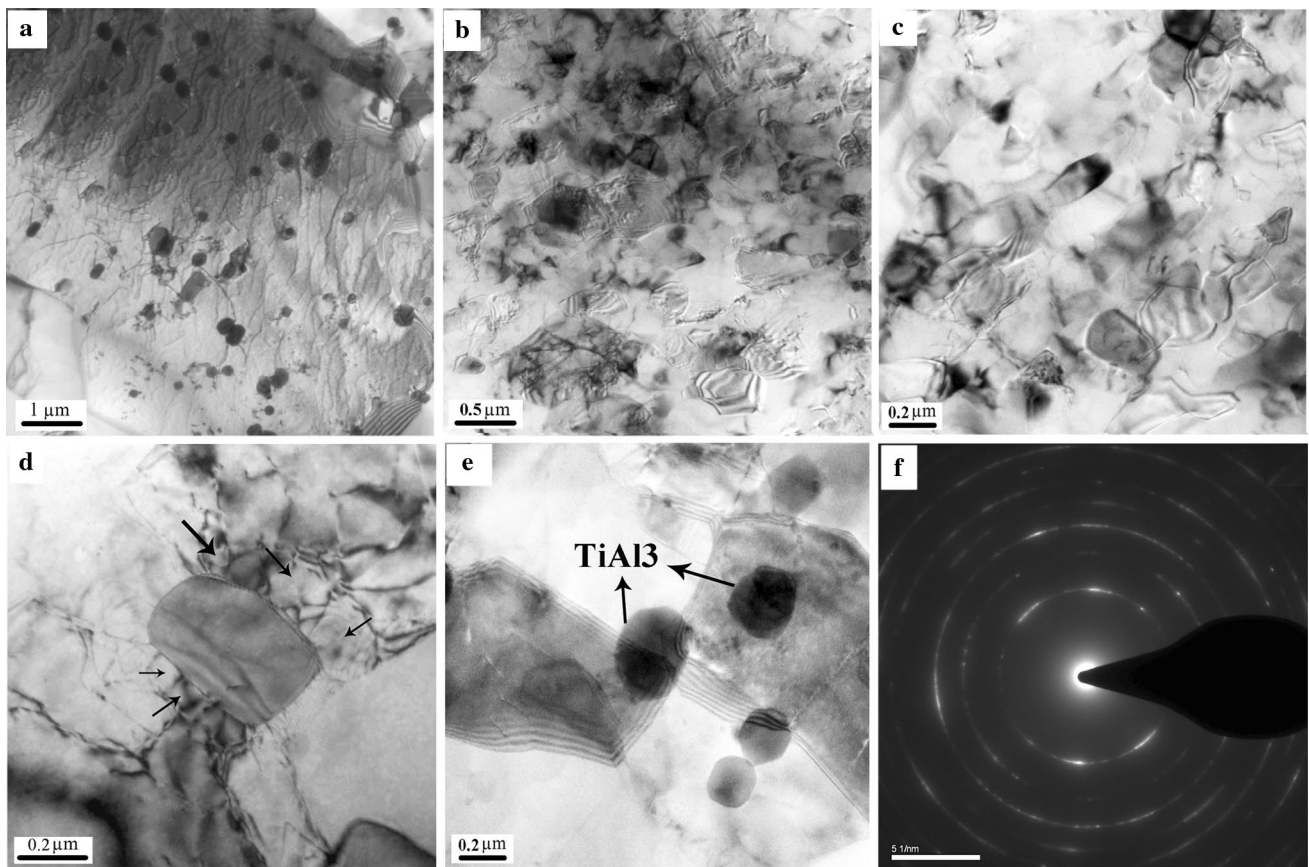
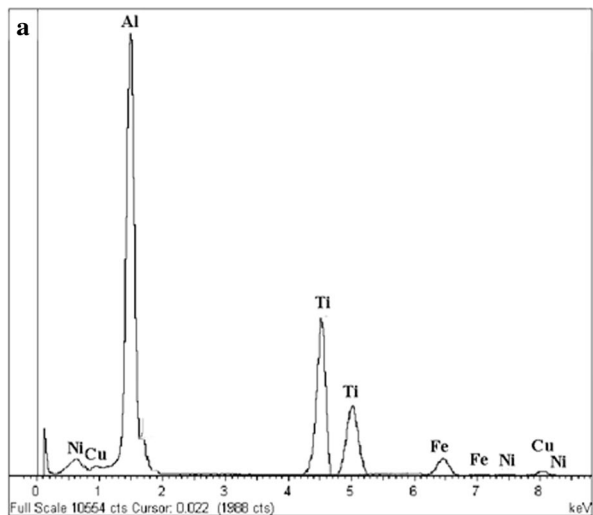


Fig. 7 TEM images of different areas of the CRB-AT-ARB5 sample with different magnifications **a–e**, the resulting SAD pattern **f**

particles has declined to nearly 200 nm (Fig. 7e). The arrows in Fig. 7d show the formation of subgrains around intermetallic particles. A diminution in the Al grain size may also be the result of the existence of the intermetallic compounds. The small and well-distributed intermetallic particles can

increase the dislocation density around these particles, which results in a smaller Al grain size. The SAD pattern (Fig. 7f) shows discrete diffraction dots on the Debye–Scherrer rings of the Al structure, signifying the appearance of a considerable number of small grains with random directions.

The chemical composition of particles shown in Fig. 7e was determined to be TiAl₃ intermetallic compound using the EDS detector of TEM equipment, and the elemental



b

Element	Peak Area	k factor	Weight%	Atomic%
Al K	138134	1.044	72.06	71.92
Ti K	7458	1.810	21.12	21.53
Ni K	21477	1.153	1.53	1.95
Fe K	11176	1.170	2.12	2.06
Cu K	813	1.366	3.17	2.54
Totals			100.00	

Fig. 8 **a** Elemental analysis, **b** elemental composition of the particles indicated in Fig. 7e

analysis and composition results presented in Fig. 8 confirm this finding. Therefore, it can be concluded that an Al matrix with a uniform distribution of TiAl₃ particles is obtained after 5 cycles of ARB procedure.

Figure 9 indicates the TEM images of the CRB-ARB5-AT sample. According to these images, as a result of annealing the sample after 5 cycles of ARB procedure at 590 °C for 2 h, the process of recovery and removal of dislocations as well as recrystallization and re-growth of Al grains have occurred in certain parts of the sample. The dislocation density of the CRB-ARB5 sample calculated using Eq. (1) was $13 \times 10^{13} \text{ m}^{-2}$, which decreased to $0.8 \times 10^{13} \text{ m}^{-2}$ due to annealing. Under these conditions, the Al grain size increased considerably. Some areas show the development of uniaxial grains as a consequence of the recrystallization process (Fig. 9a), while other areas contain columnar grains with stretched boundaries as a result of the rolling process (Fig. 9b). No subgrains could be observed inside these columnar grains after the annealing process. Figure 9b also shows the presence of TiAl₃ intermetallic particles with submicron average size.

As already mentioned, the dislocation densities were calculated using the XRD patterns of different samples. Figure 10 demonstrates the XRD patterns of initial Al, CRB, CRB-AT, CRB-AT-ARB5, and CRB-ARB5-AT samples. It can be observed that after the CRB process, the XRD pattern shows peaks corresponding to only the Al matrix and the added Ti particles, but after the CRB-AT, almost all Ti is turned into the TiAl₃ phase. In XRD patterns, the crystallite size reduction and increasing internal stresses are considered by the diffraction peak broadening. The peak broadening

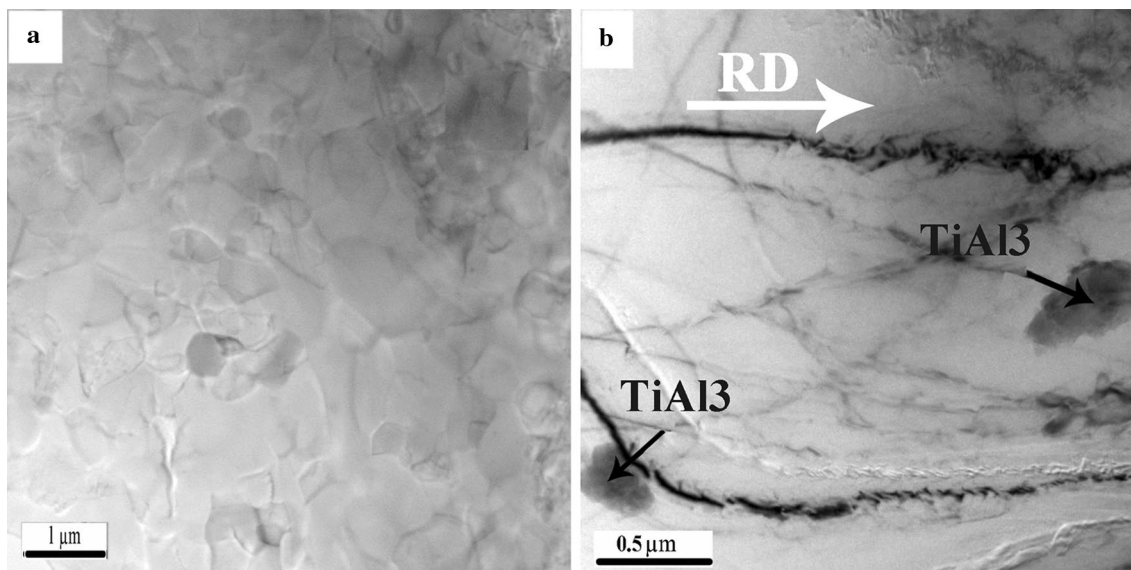


Fig. 9 **a,b** TEM images of two different areas of the CRB-ARB5-AT sample (white and black arrows showing the rolling direction and TiAl₃ intermetallic particles, respectively)

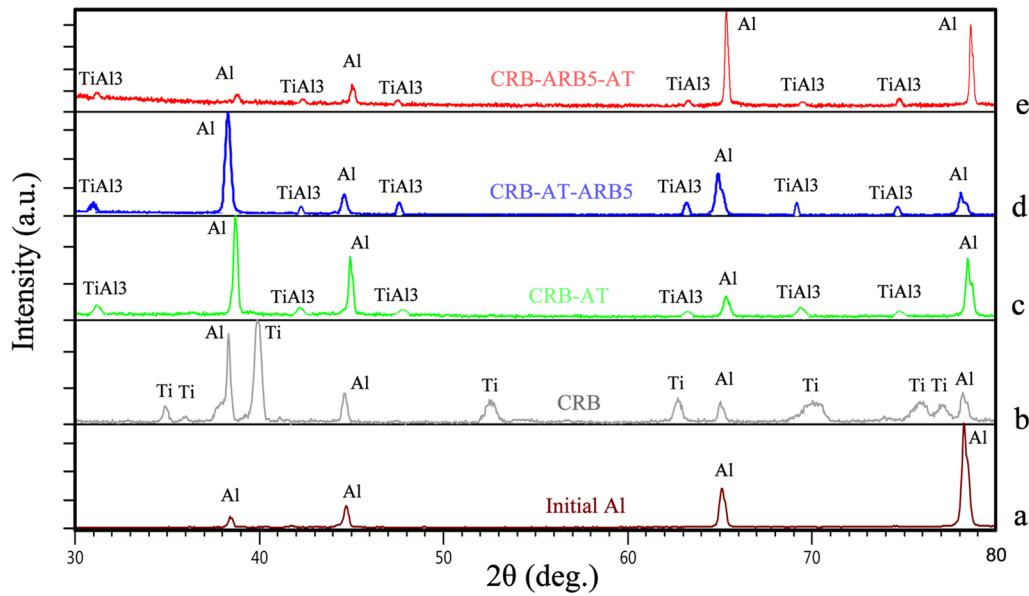


Fig. 10 XRD patterns of **a** initial Al, **b** CRB, **c** CRB-AT, **d** CRB-AT-ARB5, **e** CRB-ARB5-AT samples

value for the CRB-AT-ARB5 sample is higher than that for the CRB-ARB5-AT sample with a dislocation densities of $45 \times 10^{13} \text{ m}^{-2}$ and $0.8 \times 10^{13} \text{ m}^{-2}$, respectively. It can be reported that the grain refinement of the ARB samples by increasing the number of ARB cycles is because of the formation of the boundaries with different geometries which are arranged in parallel bundles and according to the axis of the deformation [18]. In addition, there is a shift of Al peaks toward lower diffraction angles for cold rolled samples and also toward higher diffraction angles for heat treated samples. These changes could be due to high dislocation density and internal stresses in the first group, and low lattice size for the second group.

3.3 Mechanical Properties of CRB-AT-ARB and CRB-ARB-AT Composites

The engineering stress–strain curves of the initial Al, CRB, CRB-AT and CRB-AT-ARB samples after 1 to 5 ARB cycles are demonstrated in Fig. 11. Figure 11a shows that the initial Al sample had an ultimate tensile strength of 150 MPa with an elongation of around 24%. After cold roll bonding and as a result of cold work, its ultimate strength increases to around 250 MPa, while its ductility decreases significantly. In the CRB-AT sample, although a large part of the ductility lost as a result of cold work has been recovered during the annealing process, the final ductility is still somewhat less

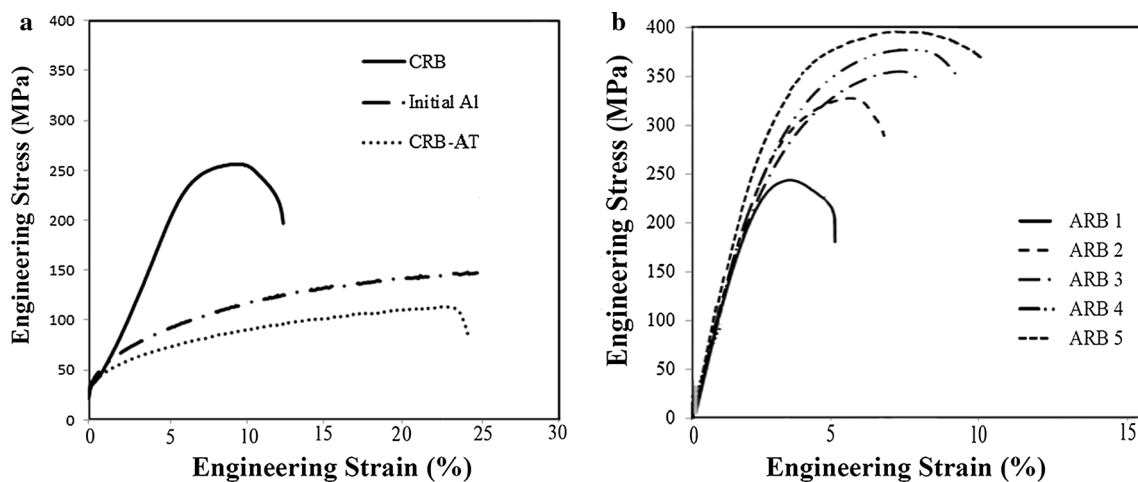


Fig. 11 Engineering stress–strain curves of **a** initial Al, CRB, and CRB-AT, **b** CRB-AT-ARB samples after 1 to 5 ARB cycles

than that of the initial Al specimen. The stress–strain curves of the CRB-AT-ARB samples after 1 to 5 ARB cycles are displayed in Fig. 11b. As illustrated, after the first cycle of the ARB procedure, ductility decreases in comparison with the CRB-AT sample, and strength increases to 240 MPa. Subsequent cycles of the ARB procedure resulted in the gradual improvement of ductility and strength, with the final strength after 5 ARB cycles reaching 400 MPa, a great value for an Al alloy. The elongation of the CRB-AT composite sample was 23%, which decreased by 4% after the first cycle of the ARB procedure. The main reason for the decrease in ductility was cold work because of rolling and high strain hardening due to a decrease in thickness and severe plastic deformation. By raising the number of ARB cycles, ductility gradually improved. Finally, the ductility of the composite with TiAl₃ particles after 5 cycles of the ARB procedure was 10%. The most important advantage of the CRB-AT-ARB composite is the improved strength after the ARB procedure. The ultimate tensile strength of this specimen after 5 cycles of the ARB process was nearly 400 MPa. In the CRB-AT-ARB5 sample, TiAl₃ was dispersed uniformly in the Al matrix with an ultrafine grain structure (Fig. 7f). Therefore, the composite containing Ti aluminide had higher strength than the Al sample manufactured using the same process without the addition of Ti powder, which has an ultimate tensile strength of 300 MPa [12, 19]. The increase in strength by growing ARB cycles can be due to increased deformation, decreased grain size, and enhanced dislocation density. The high strength of composites containing reinforcement particles indicates that the presence of TiAl₃ intermetallic particles of submicron size in the Al matrix can significantly enhance the strength of the composite. The existence of submicron intermetallic particles in the Al matrix increases the ultimate strength since the hard intermetallic phase causes the pinning of the grain boundaries

in the Al matrix (as seen in the TEM image of Fig. 7a) and prevents their movement during the ARB process [20]. This leads to expanded dislocation density of the matrix around the interface of reinforcement particles. Moreover, throughout plastic deformation, large plastic strain gradients exist near the intermetallic particles in the matrix; therefore, geometrically necessary boundaries are formed (as seen in Fig. 7a), which results in the higher strength of the matrix through the grain-boundary strengthening mechanism [21].

The engineering stress–strain curves of the initial Al and CRB, and CRB-ARB1-AT, CRB-ARB3-AT, and CRB-ARB5-AT samples are presented in Fig. 12. Figure 12a, similar to Fig. 11a, shows that CRB has increased the strength and decreased the ductility of the sample compared to the initial Al. Figure 12b shows that the strength of the sample that underwent 1 cycle of the ARB procedure before annealing was 160 MPa. By growing ARB cycles, the strength of the samples expanded, and the ultimate tensile strength of CRB-ARB5-AT was 240 MPa. Ductility also improved from 17% after 1 cycle to 20% after 5 cycles. The initial Al has an elongation of 24% and ultimate tensile strength of 150 MPa, as seen in Fig. 11a. Although annealing at 590 °C for 2 h after 5 cycles of ARB process has increased the ductility, the results indicate that annealing as the last step of the process has resulted in a reduction in strength. The strength of this specimen (240 MPa) is not considerably greater than that of the initial Al and is substantially lower than the 400 MPa of the CRB-AT-ARB5 sample (Fig. 11b). Changes in strength and microstructure are fully consistent with each other. It can be seen that as a consequence of annealing after the ARB procedure, the structure undergoes a recovery process resulting in decreased dislocation density as well as recrystallization, and finally, grain growth. This process decreases strength while improves ductility. In addition, the driving force of recrystallization is the energy stored as a result of

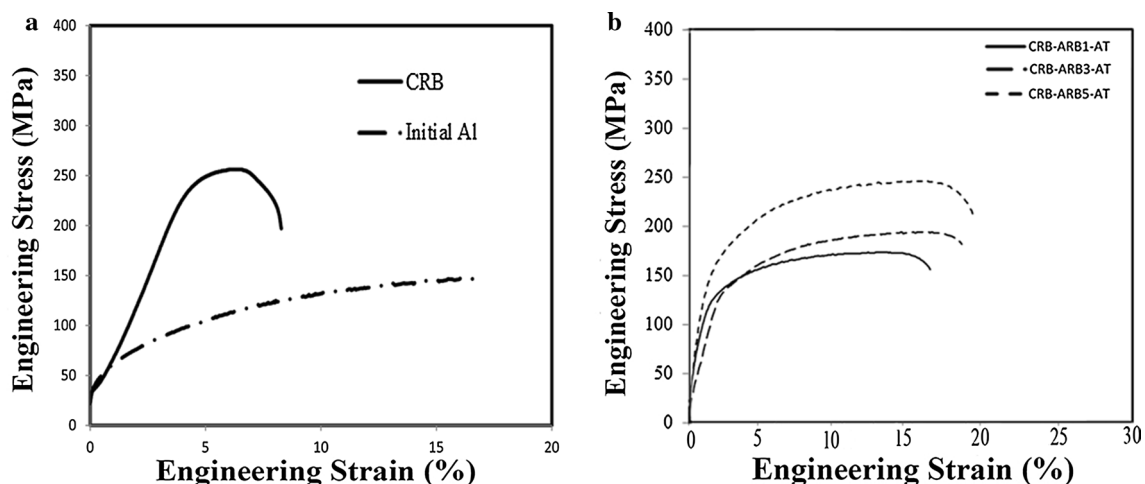


Fig. 12 Engineering stress–strain curves of **a** initial Al and CRB, **b** CRB-ARB1-AT, CRB-ARB3-AT, and CRB-ARB5-AT samples

cold work. This means that the extent of recrystallization increases with an increase in cold work, turning subgrain boundaries into main grain boundaries. Furthermore, the effect of reinforcement particles should also be considered. The sample that underwent 5 ARB cycles before annealing at 590 °C for 2 h had a smaller intermetallic particle size and a more uniform distribution of particles. This prevented grain growth, and therefore, increased the strength compared to the sample that only underwent 1 cycle before annealing at 590 °C for 2 h.

3.4 Porosity in CRB-AT-ARB and CRB-ARB-AT Composites

In these composites, Kirkendall pores are created as the intermetallic compound is formed during annealing at 590 °C for 2 h. In the CRB-AT-ARB composites, growth in ductility with enhance in ARB cycles after annealing can be related to the removal of Kirkendall pores due to the subsequent ARB rolling. This can be seen in the SEM images of the longitudinal cross-sections of the samples (normal to the TD) prepared through focused ion beam (FIB) milling (Fig. 13). The SEM images after 1 (Fig. 13a) and 5 (Fig. 13b) ARB cycles indicate a reduction in the number and size of the pores by extending ARB cycles. Furthermore, Fig. 13a displays a discontinuity in the interface of Al layers; after 5 cycles of ARB (Fig. 13b), the number of these discontinuities is significantly smaller. This shows better bonding between the layers as well as at the matrix–reinforcement phase interface, which can be an ineffective factor in decreasing porosity.

The SEM image of the CRB-ARB5-AT sample after FIB milling presented in Fig. 14 shows a high density of Kirkendall pores and their distribution in the microstructure. In these samples, since the intermetallic compound is

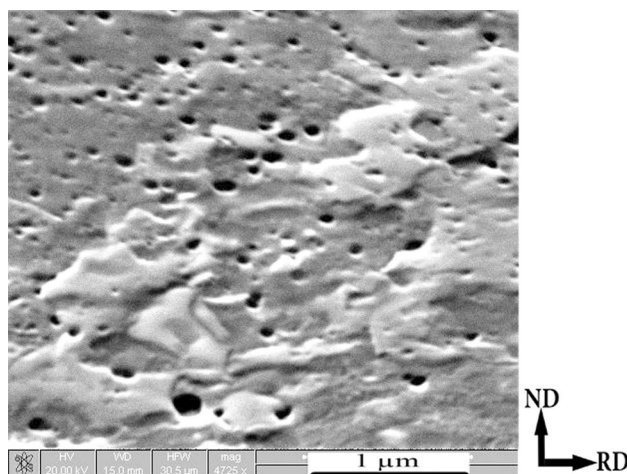


Fig. 14 SEM images of CRB-ARB5-AT sample after FIB milling

constituted at the final step of the process, the Kirkendall pores created are not removed, which reduces the strength, ductility, and density of the composite.

3.5 Nanoindentation Properties in CRB-AT-ARB and CRB-ARB-AT Composites

As shown in Fig. 15, in the CRB-AT-ARB composites, the average hardness measured using the Oliver–Pharr method [14] for the initial Al and CRB, and CRB-AT samples were 0.35, 0.45, and 0.30 GPa, respectively. The hardness evolutions indicate that the matrix hardness increment due to CRB decreases after annealing and expands with the ARB cycles. The hardness of the Al matrix was 1.21 GPa after the first cycle and reached 1.5 GPa after 5 cycles. In the ARB procedure, the presence of strain accommodation in the interface

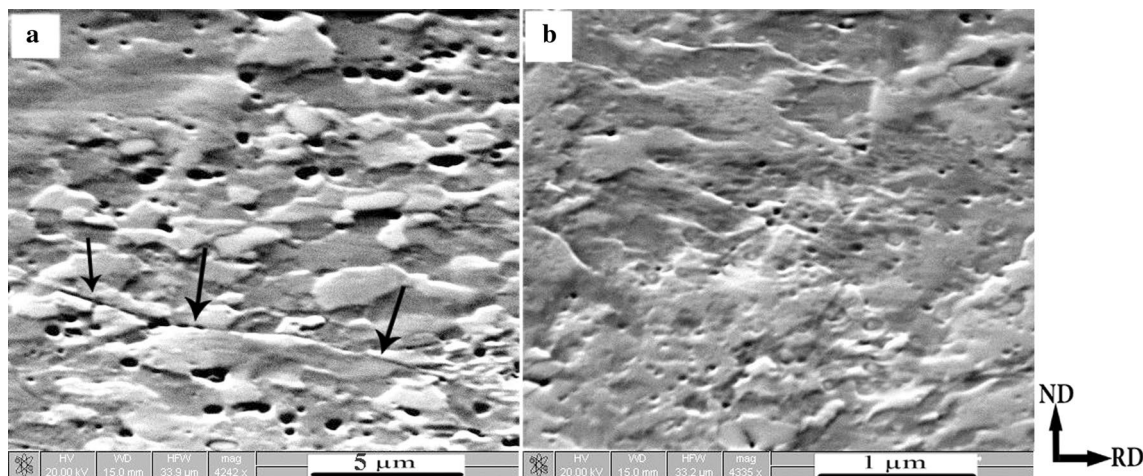


Fig. 13 SEM images of **a** CRB-AT-ARB1 (black arrows showing the interface discontinuities of Al layers), **b** ARB-AT-ARB5 samples after FIB milling

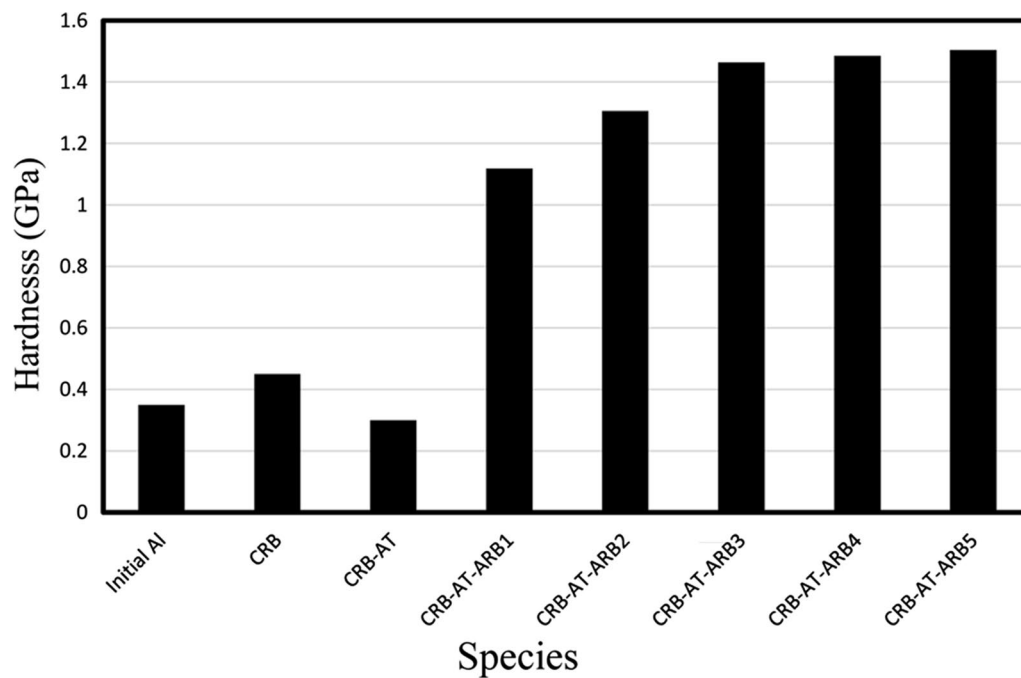


Fig. 15 Changes in the hardness of the Al matrix in the initial Al and CRB, and CRB-AT and CRB-AT-ARB samples after different ARB cycles

of the Al–intermetallic particles created interface dislocations, which in turn increased the hardness and strength of the sample [22]. Another factor affecting the increase in hardness is the presence of the oxide layer formed before the ARB process and its fracture during the ARB process, which introduces Al oxide particles to the Al matrix [23, 24]. These particles also increase dislocation density and decrease grain size. It had been informed [12] that the hardness of Al processed using the ARB method is higher than Al processed using other methods with equal strains, which is mostly a result of the existence of Al oxide particles. In general, enhance in dislocation density and decline in grain size during manufacturing processes result in higher hardness [25], but it is noticeable that the hardness of the Al matrix containing reinforcement particles is higher than the Al without these particles (which has been reported as 0.8 GPa [12]), and this can be due to a further decline in grain size because of the existence of TiAl₃ intermetallic particles. In the next step, the nanoindentation examination was used to determine the elastic moduli of different phases, and their average values are reported here. The elastic modulus of Al and Ti was measured to be 69 GPa and 210 GPa, respectively. Furthermore, the elastic modulus of TiAl₃ intermetallic particles with a hardness of 6 GPa was 141 GPa, and that of the final composite (CRB-AT-ARB5) containing 5 vol% of TiAl₃ intermetallic reinforcement particles was measured to be 82 GPa. It can be predicted that, due to the great elastic modulus of TiAl₃ particles, the Young modulus of Al-TiAl₃ composite effectively expands with growing volume fraction

of intermetallic particles [26]. Moreover, in Al-TiAl₃ composites, the elastic modulus of Al and Ti was reported to be 70 GPa and 216 GPa, respectively [27].

The elastic modulus E_c of the strengthened nanocomposite was predicted using the Halpin–Tsai equation [28]:

$$E_c = (E_m(1 + \eta qV))/(1 - qV), \quad q = \left(\left(\frac{E_p}{E_m} \right) - 1 \right) / \left(\left(\frac{E_p}{E_m} \right) + \eta \right), \quad (2)$$

in which E_m and E_p are the Young moduli of the matrix and particles measured by nanoindentation test, respectively, V is the volume fraction of the nanoparticles, and η is a constant parameter close to 1.

Therefore, in composites with a TiAl₃ particle volume fraction of 0.05, the elastic modulus predicted using Eq. (2) is around 78 GPa. These values are in reasonable relations with the findings of the nanoindentation measurements, indicating the applicability of the Halpin–Tsai prediction for the present composite.

The nanoindentation measurements for CRB-ARB-AT specimens after the first, third, and fifth ARB cycles are presented in Fig. 16. As illustrated, the hardness of Al increases to around 0.5 GPa after CRB and reaches about 0.8 GPa after the first cycle. With subsequent cycles of the ARB procedure, the hardness increases further and reaches 1.8 GPa after the fifth ARB cycle. As mentioned above, the growth in hardness with the ARB cycles is related to the improved dislocation density and decreased grain size. Furthermore, the results indicate that annealing after each ARB cycle, aimed

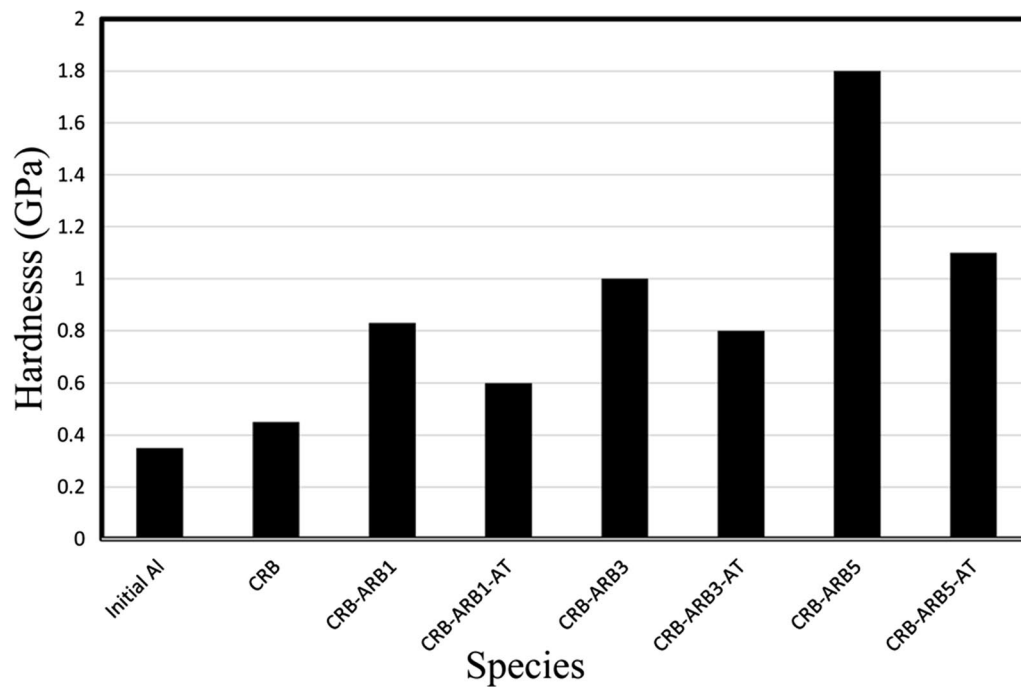


Fig. 16 Variations in the hardness of the Al matrix in the initial Al, and CRB-ARB, and CRB-ARB-AT specimens after the first, third, and fifth cycles of the ARB process

at producing intermetallic compounds, results in decreased hardness. The hardness of the sample after 5 ARB cycles and annealing at 590 °C for 2 h reaches 1 GPa. A decrease in hardness as a result of annealing is due to increased grain size as a result of the elimination of subgrains.

3.6 Strengthening Mechanisms

Al matrix composites manufactured using the CRB-AT-ARB approach showed higher strength than those fabricated using the CRB-ARB-AT method. To gain more insight into this, the

contribution of each strengthening mechanism to the CRB-AT-ARB samples at different ARB cycles is provided in Table 3.

The grain boundary strengthening defines as enhancing in yield strength (σ_y) in respect to grain size which is calculated using the Hall–Petch equation [29, 30]:

$$\sigma_y = \sigma_0 + K/\sqrt{d}, \quad (3)$$

in which σ_0 is the friction stress, d is the average grain size, and K is the strengthening coefficient, which are equal to 33 MPa and 74 MPa $\mu\text{m}^{1/2}$ for Al 1100, respectively [31].

Table 3 Calculated effects of grain boundary strengthening, strain hardening, and Orowan mechanisms compared to empirical data for CRB-AT-ARB samples

CRB-AT-ARB samples in different cycles	Al grain size (μm)	TiAl ₃ particle size (μm)	Calculated grain boundary strengthening (Eq. (3))	Dislocation density (10^{13} m^{-2}) (Eq. (1))	Strain hardening (MPa) (Eq. (4))	Orowan (MPa), (Eq. (7))	Theoretical yield strength (MPa)	Empirical yield strength (MPa)
CRB-AT-ARB1	1–5	0.7–40	76 (51%)	1.8	40 (27%)	32 (22%)	148	160
CRB-AT-ARB2	0.8–1	0.6–10	111 (54%)	4.5	48 (23%)	46 (22%)	205	210
CRB-AT-ARB3	0.5–0.8	0.5–10	127 (50%)	10.8	66 (26%)	58 (23%)	251	253
CRB-AT-ARB4	0.4–0.6	0.5–8	138 (50%)	18	82 (29%)	57 (20%)	277	284
CRB-AT-ARB5	0.2–0.5	0.2–5	150 (48%)	45	98 (31%)	60 (20%)	308	310

The increasing strength as a result of strain hardening is calculated using Taylor's equation [32]:

$$\Delta\sigma_{\text{Dis}} = M\alpha Gb\sqrt{\rho}, \quad (4)$$

where α is a constant equal to 0.24, ρ is the dislocation density, b is the Burgers vector (0.286 nm), G is the shear modulus of the matrix (24.6 GPa), and M is the Taylor constant, which is equal to 3 for polycrystalline materials with an FCC structure.

Orowan strengthening due to the intermetallic particles was estimated with the assumption of spherical particles and uniform distribution. The distance (λ) between the intermetallic particles is calculated using Eq. (5) [33]:

$$\lambda = \left[\left(\sqrt{\frac{\pi}{V}} \right) - 2 \right] \left(\sqrt{\frac{2}{3}} \right) r, \quad (5)$$

where the V is the volume fraction of TiAl₃ particles and r is their radius. The shear strength resulting from the particles is calculated using the following Eq. (6):

$$\tau_{\text{OR}} = \frac{0.81Gb}{2\pi(1-\nu)^{1/2}\lambda} \ln \left(2\sqrt{\frac{2}{3}} \frac{r}{r_0} \right), \quad (6)$$

where b is the Burgers vector (0.286 nm), G is the shear modulus of the matrix (24.6 GPa), ν is Poisson's coefficient (0.345), and r_0 is the dislocation core radius (4b). The Orowan strengthening in the tensile strength is measured using Eq. (7):

$$\sigma_{\text{OR}} = M\tau_{\text{OR}}, \quad (7)$$

where M is Taylor's coefficient, which has been previously presented.

The theoretical values of the rising yield strength because of grain boundary strengthening, strain hardening, and Orowan mechanism were calculated using Eqs. (3), (4), and (7), respectively. The experimental results of the tensile strength were eradicated from the stress–strain curves of these specimens (Fig. 11b) and are presented in the final column of Table 3. The results indicate that by raising ARB cycles, the effect of each of the three mechanisms as well as the theoretical and experimental values of yield strength increase. To calculate the growth in yield strength as a consequence of grain boundary strengthening, the average grain size of the Al matrix (as observed in the TEM) was used. The strength caused by this mechanism in the CRB-AT sample after the first cycle was 76 MPa, which increased with the ARB cycles and obtained 150 MPa after the 5 cycles of ARB. Using the dislocation density values previously calculated using Eq. (7) and presented in Table 3, the share of the strain hardening mechanism was calculated, which increased from 40 MPa after the 1 cycle of ARB to 98 MPa after the

fifth ARB cycle. The contribution of the Orowan mechanism also improved with the ABR cycles resulting from a decrease in the size of and spacing between the reinforcement particles. In addition, in all CRB-AT-ARB samples and for all ARB cycles, the grain boundary strengthening mechanism had the most considerable contribution to the yield strength; say in the sample that underwent 5 cycles of ARB process, around 48% of the yield strength was due to this mechanism. Therefore, most of the improvement in the strength of Al-TiAl₃ composite is because of a decrease in Al grain size in addition to the existing TiAl₃ intermetallic particles in the Al matrix.

The results presented in Table 3 show that the theoretically calculated yield strength values are slightly less than the experimental values. This difference can be explained by factors such as the lack of uniformity in the distribution of particles in the first ARB cycle, the bonding conditions between the Al/Al and Al/intermetallic particle layers, and the lack of consideration of the strengthening resulting from the growth in the elastic modulus of the matrix and reinforcement particles [34]. As already stated, the availability of reinforcement particles results in the activation of dislocation sources and the formation of Orowan loops. The TEM image presented in Fig. 17 shows the formation of Orowan loops in part of the microstructure of the CRB-AT-ARB sample after the 4th ARB cycle. Based on Fig. 17a, in various parts of the microstructure, dislocations are present around the intermetallic particles as Orowan loops; this can be seen more clearly in Fig. 17b, c. This behavior is commonly observed in Al alloys containing semi-coherent particles [35].

4 Conclusions

In this article, Al-matrix composites with TiAl₃ intermetallic reinforcement particles were manufactured using different rolling and annealing methods from Al 1100 sheets and pure Ti powder, and their microstructures and mechanical properties were studied. The overall conclusions according to the results of the experiments are as follows:

1. CRB, annealing, and finally, up to 5 cycles of ARB process on Al sheet–Ti powder–Al sheet composites led to forming an Al-matrix composite with an ultrafine grain matrix of an average grain size of around 500 nm and uniform distribution of TiAl₃ intermetallic particles of an average size of around 200 nm.
2. The presence of intermetallic reinforcement particles resulted in a further decline grain size due to enhance in dislocation density and the resulting suitable nucleation locations for subgrains.

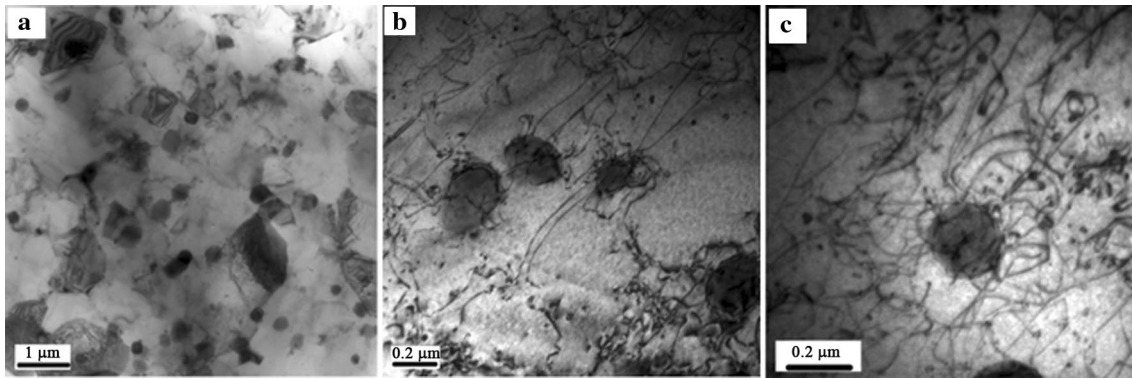


Fig. 17 TEM images exhibiting the formation of Orowan loops in different areas **a-c** of the CRB-AT-ARB4 sample

3. The strength of the composite manufactured using CRB–annealing–ARB process grows with ARB cycles and finally, reaches 400 MPa.
4. The strengthening of the Al-TiAl₃ composite is primarily due to reducing in the Al matrix's grain size and the presence of TiAl₃ intermetallic particles.
5. Microstructural investigation of the composite manufactured using the CRB-ARB-annealing process showed that the resulting Al matrix obtained after ARB and annealing has large, micron-sized grains with a large size distribution of intermetallic particles ranging between 0.2 and 50 μm.
6. Annealing before the ARB process generated the development of a compact layered structure with little porosity, and high strength and hardness, while annealing after the ARB process resulted in increased porosity, decreased strength and hardness, and a uniaxial grain structure.
7. The Al-matrix composite with TiAl₃ intermetallic reinforcement particles manufactured using annealing before the ARB process has attractive mechanical properties, while the formation of the intermetallic compound through annealing after the ARB process reverts some of the last changes and decreases the improvement in mechanical properties created through severe plastic deformation.

References

- [1] R.S. Rana, R. Purohit, S. Das, *IJSER* **3**, 1 (2012)
- [2] T.W. Clyne, in *Encyclopedia of Materials: Science and Technology*, Composites: MMC, CMC, PMC, ed. by A. Mortensen, (Elsevier, New York, 2001), p. 1
- [3] T. Massalski (ed.), *binary alloy phase diagrams*, (American society for metals, 1986)
- [4] J. Heathcote, G. Odette, G. Lucas, R. Rowe, D. Skelly, *Acta Mater.* **44**, 2489 (1996)
- [5] D. Lesuer, C. Syn., *Metallic laminates for engine applications*. Paper presented at 8th CIMTEC World Ceramics Congress and Forum on New Materials, Florence, Italy, 1994
- [6] Y. Saito, N. Tsuji, H. Utsunomiya, T. Sakai, R.G. Hong, *Scr. Mater.* **39**, 1221 (1998)
- [7] Y. Saito, H. Utsunomiya, N. Tsuji, T. Sakai, *Acta Mater.* **47**, 579 (1999)
- [8] N. Tsuji, Y. Ito, Y. Saito, Y. Minamino, *Scr. Mater.* **47**, 893 (2002)
- [9] J. Oh, S.G. Pyo, S. Lee, N.J. Kim, *J. Mater. Sci.* **38**, 3647 (2003)
- [10] J.G. Luo, V.L. Acoff, *Mater. Sci. Eng. A* **379**, 164 (2004)
- [11] G.P. Chaudhari, V.L. Acoff, *Intermetallics* **18**, 472 (2010)
- [12] Z. Yazdani, M.R. Toroghinejad, H. Edris, A.H.W. Ngan, *J. Alloys Compd.* **747**, 217 (2018)
- [13] F.V. Loo, G. Rieck, *Acta Metall. Mater.* **21**, 61 (1973)
- [14] W.C. Oliver, G.M. Pharr, *J. Mater. Res.* **7**, 1564 (1992)
- [15] Z. Yazdani, M.R. Toroghinejad, H. Edris, A.H.W. Ngan, *T. Indian I. Metals* **71**, 2497 (2018)
- [16] R. Jamaati, M. R. Toroghinejad, *Mater. Des.* **31**, 4816 (2010)
- [17] R.E. Smallman, K.H. Westmacott, *Philos. Mag.* **2**, 669 (1957)
- [18] D. Rahmatabadi, R. Hashemi, B. Mohammadi, T. Shojaee, *Mater. Sci. Eng. A* **708**, 301 (2017)
- [19] R. Guan, D. Tie, *Acta Metall. Sin. -Engl. Lett.* **30**, 409 (2017)
- [20] H.R. Lin, Y.Z. Tian, S.J. Sun, *Acta Metall. Sin. -Engl. Lett.* **34**, 925 (2021)
- [21] C.Y. Liu, R. Jing, Q. Wang, B. Zhang, Y.Z. Jia, M.Z. Ma, R.P. Liu, *Mater. Sci. Eng. A* **558**, 510 (2012)
- [22] N. Jia, M.W. Zhu, Y.R. Zheng, T. He, X. Zhao, *Acta Metall. Sin. -Engl. Lett.* **28**, 600 (2015)
- [23] M. Alizadeh, M.H. Paydar, F.S. Jazi, *Compos. Part B: Eng.* **44**, 339 (2013)
- [24] R. Jamaati, M.R. Toroghinejad, J. Dutkiewicz, J.A. Szpunar, *Mater. Des.* **35**, 37 (2012)
- [25] A. Mostafapor, V. Mohammadinia, *Acta Metall. Sin. -Engl. Lett.* **29**, 735 (2016)
- [26] C.J. Hsu, C.Y. Chang, P.W. Kao, N.J. Ho, C.P. Chang, *Acta Mater.* **54**, 5241 (2006)
- [27] M. Nakamura, K. Kimura, *J. Mater. Sci.* **26**, 2208 (1991)
- [28] D. Hull, T.W. Clyne, *An Introduction to Composite Materials* (Cambridge University, Cambridge, 1996), p. 66
- [29] E.O. Hall, The deformation and aging of mild steel. *Proc. Phys. Soc. London B* **64**, 747 (1951)
- [30] N.J. Petch, *J. Iron Steel Inst.* **25**, 174 (1953)
- [31] C.Y. Yu, P.W. Kao, C.P. Chang, *Acta Mater.* **53**, 4019 (2005)
- [32] B. Li, A. Godfrey, Q. Meng, Q. Liu, N. Hansen, *Acta Mater.* **52**, 1069 (2004)
- [33] J.W. Martin, *Micromechanisms in Particle Hardened Alloys* (Cambridge University, Cambridge, 1980), p. 60
- [34] R. Casati, M. Vedani, *Metals* **4**, 65 (2014)
- [35] F.J. Humphreys, M. Hatherly, *Recrystallization and Related Annealing Phenomena* (Elsevier, Oxford, 2004)